ORIGINAL PAPERS

Artificial photosynthesis: photoanodes based on polyquinoid dyes onto mesoporous tin oxide surface

Giulia Alice Volpato[1] · Elena Colusso[2] · Lorenzo Paoloni[3] · Mattia Forchetta[4] · Francesco Sgarbossa[3] · Vito Cristino[5] · Marco Lunardon[1] · Serena Berardi[5] · Stefano Caramori[5] · Stefano Agnoli[1] · Federica Sabuzi[4] · Paolo Umari[3] · Alessandro Martucci[2] · Pierluca Galloni[4] · Andrea Sartorel[1]

Abstract

Dye-sensitized photoelectrochemical cells represent an appealing solution for artificial photosynthesis, aimed at the conversion of solar light into fuels or commodity chemicals. Extensive efforts have been directed towards the development of photoelectrodes combining semiconductor materials and organic dyes; the use of molecular components allows to tune the absorption and redox properties of the material. Recently, we have reported the use of a class of pentacyclic quinoid organic dyes (KuQuinone) chemisorbed onto semiconducting tin oxide as photoanodes for water oxidation. In this work, we investigate the effect of the SnO_2 semiconductor thickness and morphology and of the dye-anchoring group on the photoelectrochemical performance of the electrodes. The optimized materials are mesoporous SnO_2 layers with 2.5 µm film thickness combined with a KuQuinone dye with a 3-carboxylpropyl-anchoring chain: these electrodes achieve light-harvesting efficiency of 93% at the maximum absorption wavelength of 533 nm, and photocurrent density J up to 350 µA/cm^2 in the photoelectrochemical oxidation of ascorbate, although with a limited incident photon-to-current efficiency of 0.075%. Calculations based on the density functional theory (DFT) support the role of the reduced species of the KuQuinone dye via a proton-coupled electron transfer as the competent species involved in the electron transfer to the tin oxide semiconductor. Finally, a preliminary investigation of the photoelectrodes towards benzyl alcohol oxidation is presented, achieving photocurrent density up to

Giulia Alice Volpato and Elena Colusso equally contributed.

✉ Paolo Umari
paolo.umari@unipd.it

✉ Alessandro Martucci
alex.martucci@unipd.it

✉ Pierluca Galloni
galloni@scienze.uniroma2.it

✉ Andrea Sartorel
andrea.sartorel@unipd.it

1 Department of Chemical Sciences, University of Padova, Via F. Marzolo 1, 35131 Padua, Italy

2 Department of Industrial Engineering and INSTM, University of Padova, F. Marzolo 9, 35131 Padua, Italy

3 Department of Physics and Astronomy, University of Padova, Via F. Marzolo 8, 35131 Padua, Italy

4 Department of Chemical Science and Technologies, University of Rome "Tor Vergata", Via della Ricerca Scientifica, snc, 00133 Rome, Italy

5 Department of Chemical and Pharmaceutical Sciences, Centro Interuniversitario per la Conversione Chimica dell'Energia Solare (SolarChem), Sez. di Ferrara, University of Ferrara, Via L. Borsari 46, 44121 Ferrara, Italy

90 µA/cm^2 in acetonitrile in the presence of *N*-hydroxysuccinimide and pyridine as redox mediator and base, respectively. These results support the possibility of using molecular-based materials in synthetic photoelectrochemistry.

Graphic abstract
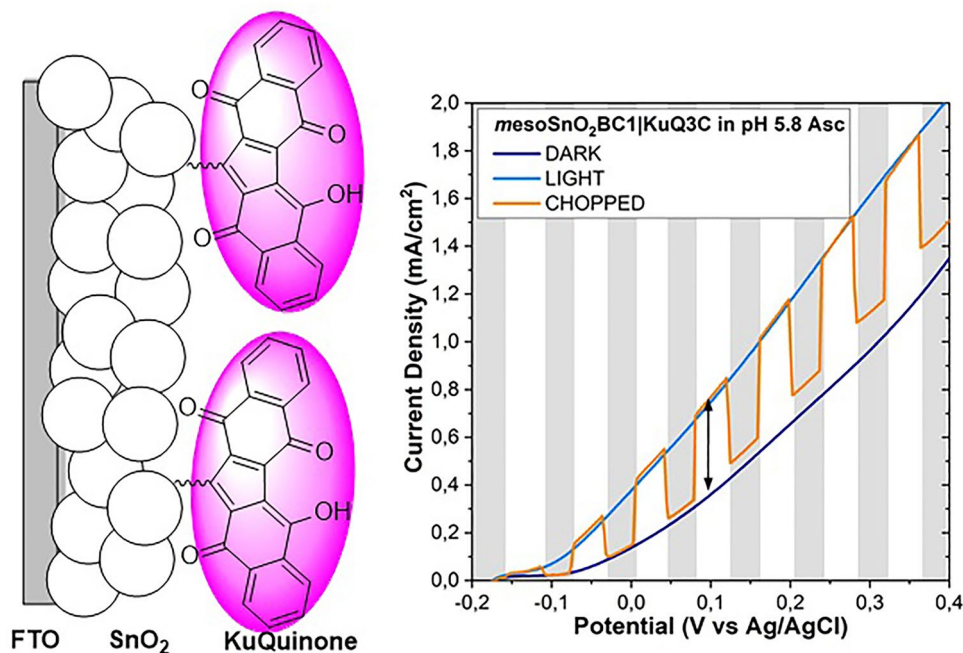
Abbreviations

PECs	Photoelectrochemical cells
PCET	Proton-coupled electron transfer
LHE	Light-harvesting efficiency
DFT	Density-functional theory
FE-SEM	Field emission scanning electron microscopy
LSV	Linear sweep voltammetry

1 Introduction

Artificial photosynthesis is considered an appealing strategy to convert the massive, inexhaustible amount of radiant energy received from the sun into solar fuels or commodity chemicals. The basic principles of photosynthesis are the generation of light-induced charge separation and the use of the photogenerated charge carriers to promote redox reactions, typically involving the activation of small molecules.

Nowadays, the proposed technologies to develop the photosynthetic processes are based on (i) photovoltaic modules coupled to electrolyzers, (ii) photoelectrochemical cells (PECs) [1] or (iii) mixed colloids (particulate materials) [2], listed in order of increasing appeal for scalability purposes.

PECs are still widely investigated due to their well-established technology. These are based on two (photo)electrodes connected by an external circuit, with the oxidation and reduction reactions that take place at the anodic and cathodic compartment, respectively. Importantly, the PEC setup allows to develop independently the anodic and cathodic compartments. The first PEC prototype was developed in 1967 by Fujishima and Honda [3] and was constituted by a titanium oxide semiconductor photoanode and a platinum cathode, employed for water splitting into oxygen (from anodic water oxidation) and hydrogen (from cathodic proton reduction). This seminal report inspired the subsequent investigation of other semiconductors for both compartments (n-type semiconductors for the anode, p-type semiconductors for the cathode).

Following a molecular-oriented strategy, important efforts have been dedicated to the development of dye-sensitized (DS) PECs [4–6], by combining suitable chromophores with semiconductors, to enlarge the absorption features of the electrodes and maximize solar light absorption. Besides the absorption properties, the dyes need to display suitable energy levels to allow the photoinduced electron transfer with the semiconductor, and sufficient stability under operative conditions.

Recently, the research in the field of DS-PECs has been intensively focused on the development and on the application of novel dyes for the photoanodic compartment; seminal work by Mallouk and co-workers reported the use of ruthenium(II) tris(bipyridine) dyes [7]; subsequent reports

proposed the use of organic chromophores, which appears particularly promising given the possibility of tuning the electronic and redox properties, while avoiding the use of rare metals. Porphyrinoid derivatives [8–12], BODIPY [13], perylenes [14–18], triarylamines [19, 20], and polymeric films [21–23] have thus been investigated, mainly towards water oxidation to oxygen.

In a recent contribution, we proposed the use of pentacyclic quinoid organic dyes (KuQuinone or KuQ, from the structure analogy with natural quinones in vitamin K_1 and bis-coenzyme Q_0) [24–28] chemisorbed onto tin oxide (SnO_2) surfaces for photoelectrochemical water oxidation in combination with a ruthenium polyoxometalate catalyst [29]. Peculiar features of this class of KuQuinone dyes are the absorption in the visible region (up to 600 nm, ε ca 1.5×10^4/M cm), a highly oxidizing excited state (E KuQ*/ KuQ$^-$ up to 2 V vs normal hydrogen electrode, NHE), and the ability to manage proton-coupled electron transfer (PCET) [29].

In this work, we investigate the functional parameters that affect the dye chemisorption and the photoelectrochemical performance of SnO_2|KuQuinone electrodes towards the oxidation of ascorbate as a benchmark reaction. We focus in particular on the morphology and thickness of the SnO_2 semiconductor, and on the chemical nature of the linker of the dye. Calculations based on the density functional theory (DFT) provide a mechanistic analysis of the electron transfer from the KuQuinone dye to the SnO_2 semiconductor layer along the photoelectrochemical process, and support the involvement of the reduced species of the dye, through a reductive quenching with ascorbate via a PCET mechanism. Finally, we explore the potential of SnO_2|KuQuinone towards the photoelectrochemical oxidation of benzyl alcohol, as a model substrate for the oxidation of alcohols, which retains significant interest for the preparation of a multitude of commodity chemicals.

2 Results and discussion

Scheme 1 represents the overall assembly of photoelectrodes presented in this work. Different preparation of the tin oxide layer and different linkers of the KuQuinone dye have been considered to optimize the light-harvesting efficiency (LHE) and photocurrent density (J) towards the photoelectrochemical oxidation of ascorbate as a probe reaction.

KuQ3C, KuQ8C and KuQ3P have been synthesized following previously reported procedures [26, 30]. The general protocol for KuQuinones synthesis involves a one-pot process, in which a bromoalkane reacts with two equivalents of 2-hydroxy-1,4-naphthoquinone in dimethylsulphoxide (DMSO), in the presence of an excess of cesium carbonate base and ferrocene in catalytic amount [25]. Such reaction
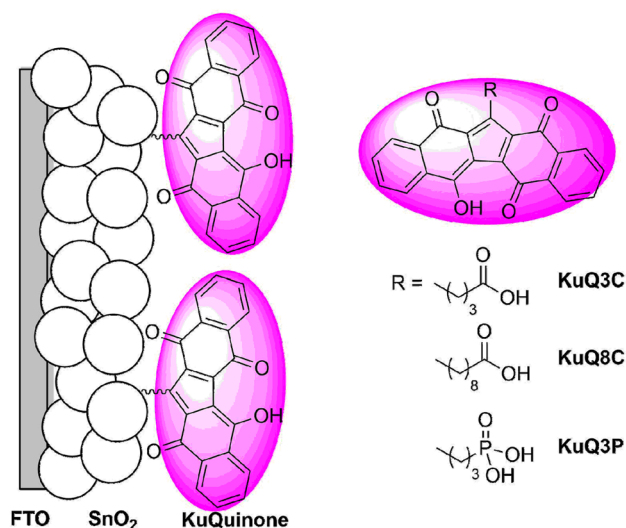

Scheme 1 Schematic representation of photoanodes developed in this work. A conductive fluorine-doped tin oxide (FTO) slide is covered with tin oxide (SnO_2) layer; KuQuinone dyes are 1-(3-carboxypropyl)KuQuinone (KuQ3C), 1-(8-carboxyoctyl)KuQuinone (KuQ8C) and 1-[3-(dihydroxyphosphonyl)propyl]KuQuinone (KuQ3P)

leads to the formation of the pentacyclic quinoid compound bearing the alkyl side chain that can be exploited to introduce carboxylic or phosphonic acid pendants, needed for anchoring the dye to oxide surfaces. However, the mentioned conditions are unsuitable with ω-bromoalkylcarboxylic or ω-bromoalkylphosphonic acid reagents, since intramolecular substitution reaction prevalently occurs. Therefore, the synthesis of KuQ3C, KuQ8C and KuQ3P has been easily accomplished by hydrolysis of the corresponding esters, synthesized starting from the appropriate ω-bromoalkyl esters (Scheme 2) [26].

The nature of the alkyl side chain does not impact significantly on the optical properties of the three dyes, which are ascribed to the extended conjugated system [27]; the UV–Vis absorption spectra in organic solvent are characterized by two vibronic components at $\lambda_1 \sim 532$ nm ($\varepsilon \sim 1.3 \times 10^4$/M cm) and at $\lambda_2 \sim 566$ nm ($\varepsilon \sim 1.5 \times 10^4$/M cm).

3 Optimization of tin oxide semiconductor

Tin oxide (in mesoporous form meso-SnO_2) [31, 32], deposited onto conductive fluorine tin oxide (FTO) slides, was previously selected as the optimal semiconductor for coupling with KuQ dyes, given the prompt and efficient chemisorption of KuQ via carboxylic functions, and due to the lower energy of SnO_2 conduction band with respect to other semiconductors [33–35] that favour light-induced electron injection from the KuQ dye.
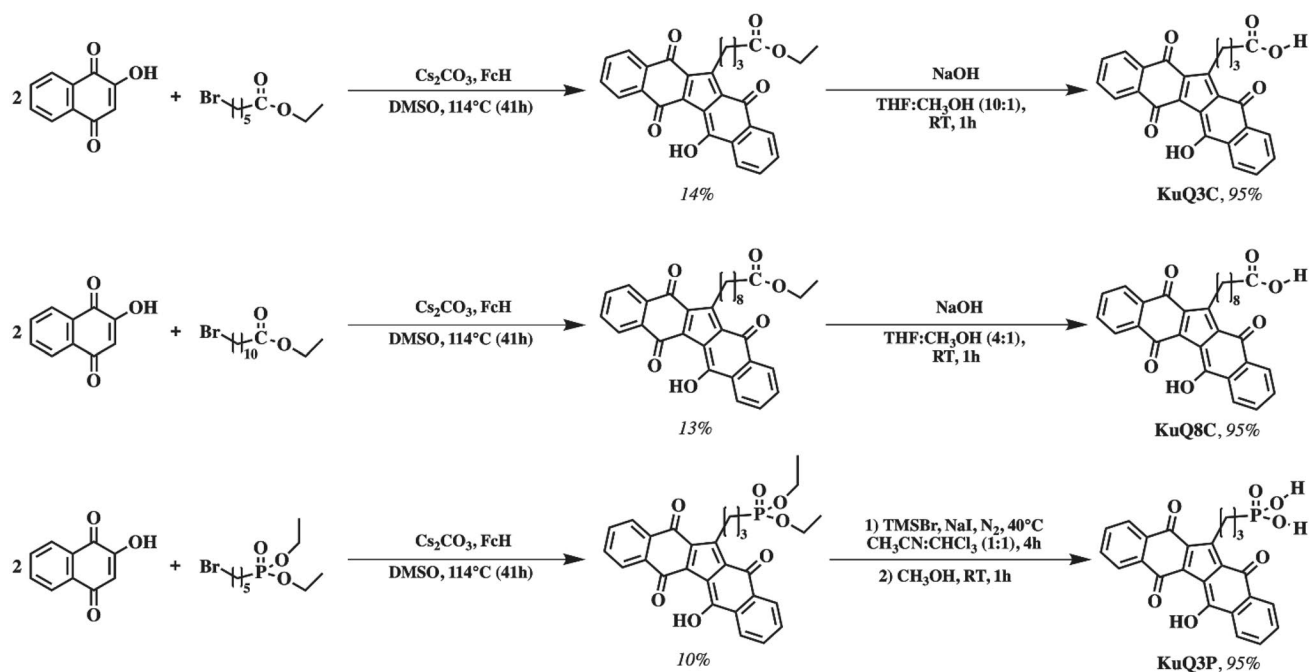
Scheme 2 Synthesis of KuQ3C, KuQ8C and KuQ3P

In the SnO₂|KuQ photoelectrodes, the morphology and the thickness of the SnO₂ semiconductor layer are expected to impact the overall performance in terms of the amount of chemisorbed dye (and as a consequence, on the light-harvesting efficiency of the electrode, LHE), but also of charge carrier transport (an excessive thickness of the film can favour recombination and thus reduce the overall photocurrent response [36]). Morphologies such as nanorods or nanotubes, in particular if perpendicularly grown on the conductive substrate, are known to have higher charge transport efficiencies with respect to nanoparticle-based films, due to the considerably lower amount of grain boundaries (or defects in general), which act as recombination centers [37–41]. On the other hand, nanoparticles-based mesoporous structures are characterized by high surface areas, resulting in enhanced light-harvesting efficiencies. The thickness of the film also affects charge transport, since recombination may become predominant for excessive thickness of the film, thus reducing the overall photocurrent response [36]. Therefore, we investigated both mesoporous nanostructured SnO₂ films of various thicknesses and vertically oriented SnO₂ nanorods (SnO₂ NRs) as possible substrates for the optimization of KuQ-sensitized photoanodes.

We prepared SnO₂ substrates with different procedures, and in particular:

(i) Meso-SnO₂ via blade coating (BC) of a paste of colloidal SnO₂ nanoparticles (ca 10 nm size, 15% w/w in aqueous solution containing 4% w/w acetic acid

and a 7% w/w of a polyethyleneglycol bisphenol A epichlorohydrin copolymer), followed by sintering up to 500 °C: these electrodes are further indicated as BCn, where n indicates the number of tape layers used as spacer for blade coating of the colloidal paste. For BC1 electrodes, dilution of the paste was also exploited to target thinner films: these electrodes are indicated as BC1_x, where x indicates the level of dilution of the paste (e.g. BC1_0.83 stands for 83% diluted paste, obtained by mixing five parts of the paste and one part of MilliQ water; BC1_0.66 stands for 66% diluted paste, obtained by mixing two parts of the paste and one part of MilliQ water). The BC procedure was employed to target SnO₂ semiconductor thickness above 1 μm.

(ii) Meso-SnO₂ via spin coating of a 40% diluted SnO₂ paste (mixing 3 parts of the original paste and 4 parts of Milliq water) and sintering up to 500 °C; these electrodes are indicated as SCn, where n indicates the number of subsequent spin-coating depositions; this procedure was followed to target semiconductor thickness of hundreds of nm.

(iii) Vertically oriented SnO₂ nanorods (SnO₂ NRs), via hydrothermal synthesis from SnCl₄ precursor [41].

Details of the experimental procedures are reported in the experimental section and in the Supporting Information.

Meso-SnO₂: The field emission scanning electron microscopy (FE-SEM) images (top view of the films) of a typical

a

b
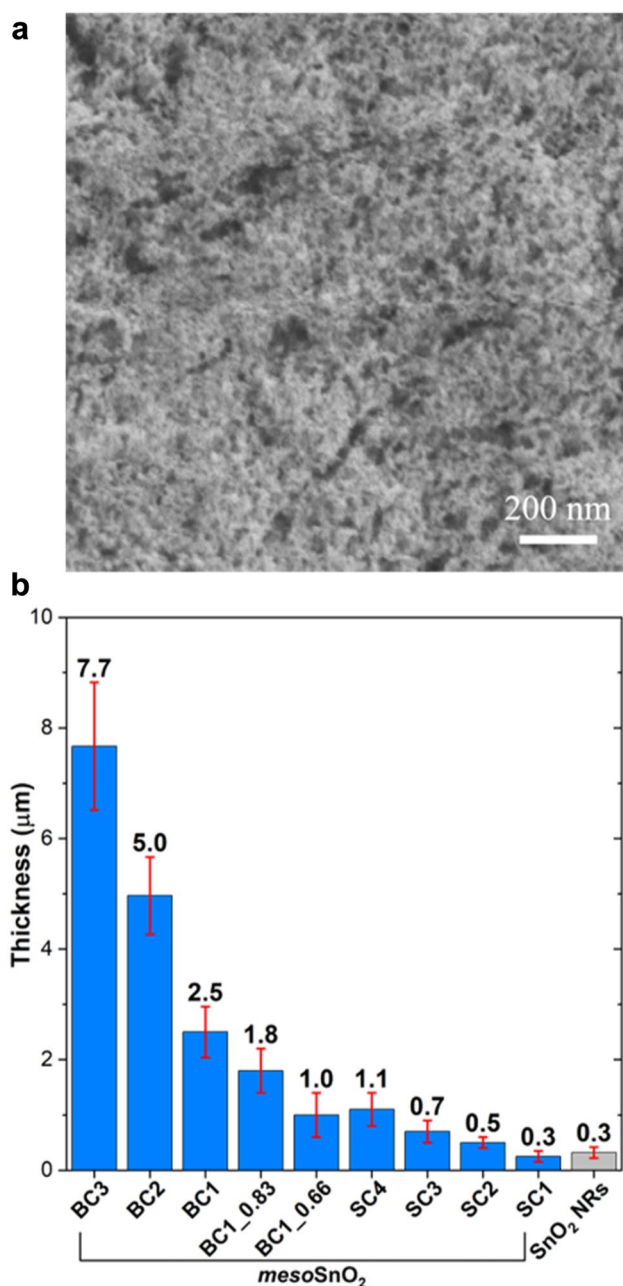
Fig. 1 a Representative SEM image of meso-SnO$_2$ electrode (BC1 sample, top view of the film). **b** Thickness of the SnO$_2$ electrodes as provided by profilometry analysis

meso-SnO$_2$ BC film are shown in Figs. 1 and S1 in Supporting Information. Meso-SnO$_2$ films are characterized by a 3D porous structure, with good interconnectivity between the particles and a high degree of porosity. The different deposition methods do not influence the final morphology: a similar mesoporous structure was observed for both BC and SC samples (compare Figs. S1, S2 in the SI). The pores sizes were estimated between 10 and 40 nm in diameter from SEM images. The crystalline structure of the meso-SnO$_2$

samples was analyzed by X-ray diffraction (Fig. S3). All diffraction peaks correspond to the tetragonal crystalline phase of SnO$_2$ (JCPDS card, No. 41-1445), and no other crystalline by-products were detected. The grain size was calculated as 9.24 nm by the Scherrer equation. By combining these two preparation strategies, the thickness of the meso-SnO$_2$ layer was tuned from about 300 nm (SC1 electrodes) above 7 μm (BC3 electrodes), Fig. 1. X-ray and ultraviolet photoemission spectroscopy (XPS, UPS) were performed on meso-SnO$_2$ BC1 film as a representative sample (Fig. S4). The line shape analysis of the Sn 3d region (Fig. S4a) evidenced the unique presence of the Sn^{4+} component ($3d_{5/2}$, 487 eV) [42–44]; consistently, the O–Sn^{4+} component (530.9 eV) [42, 45] was observed in the O 1s region (Fig. S4b). The presence of Sn^{4+} oxide phase was further and unequivocally supported by the characteristics of the Sn 4d photoemission line and Sn MNN Auger spectrum (acquired by XPS) and of the valence band region (acquired through UPS measurements) [43, 44]. The binding energy of 26.7 eV shown by the Sn 4d line, coupled to the characteristic fingerprint of the valence band with the most prominent peak at 4.8 eV given by the O 2p contribution (Fig. S4d) and the intense transition positioned at a kinetic energy of 432.2 eV of the Sn MNN Auger spectrum (Fig. S4c), both confirm the sole presence of SnO$_2$ [43–45].

SnO$_2$ NRs: Vertically aligned SnO$_2$ rods with a square section grew directly on the FTO substrate according to the reported procedure [41]. The average width is about 50 nm, as determined from SEM images (Fig. S5), with a thickness of about 300 nm from profilometry analysis. The nanorods are crystalline, with a preferential orientation along the (100) direction (see XRD measurements, Fig. S6 in Supporting Information). The XPS and UPS analyses (Fig. S7) confirm the unique presence of the Sn^{4+} oxidation state (see previous discussion).

4 Anchoring of KuQ3C dye onto SnO$_2$ and photoelectrochemical oxidation of ascorbate

The SnO$_2$ electrodes were then employed for chemisorption of the KuQ3C dye exploiting the carboxylic linker (Scheme 1), by soaking overnight of the electrodes in a 0.13 mM solution of KuQ3C in tetrahydrofuran (dichloromethane, where KuQ3C is soluble, can also be used to give electrodes with identical properties) [29]. Remarkably, due to the basicity of SnO$_2$, the enol group of KuQ3C was deprotonated to its enolate form during the soaking procedure (accordingly, the resulting photoanodes appear orange coloured, which is a clear indication of the formation of the enolate, see Fig. S8) [29]; when dipped into acidic aqueous medium (aqueous sulphuric acid, pH 2), the photoanodes
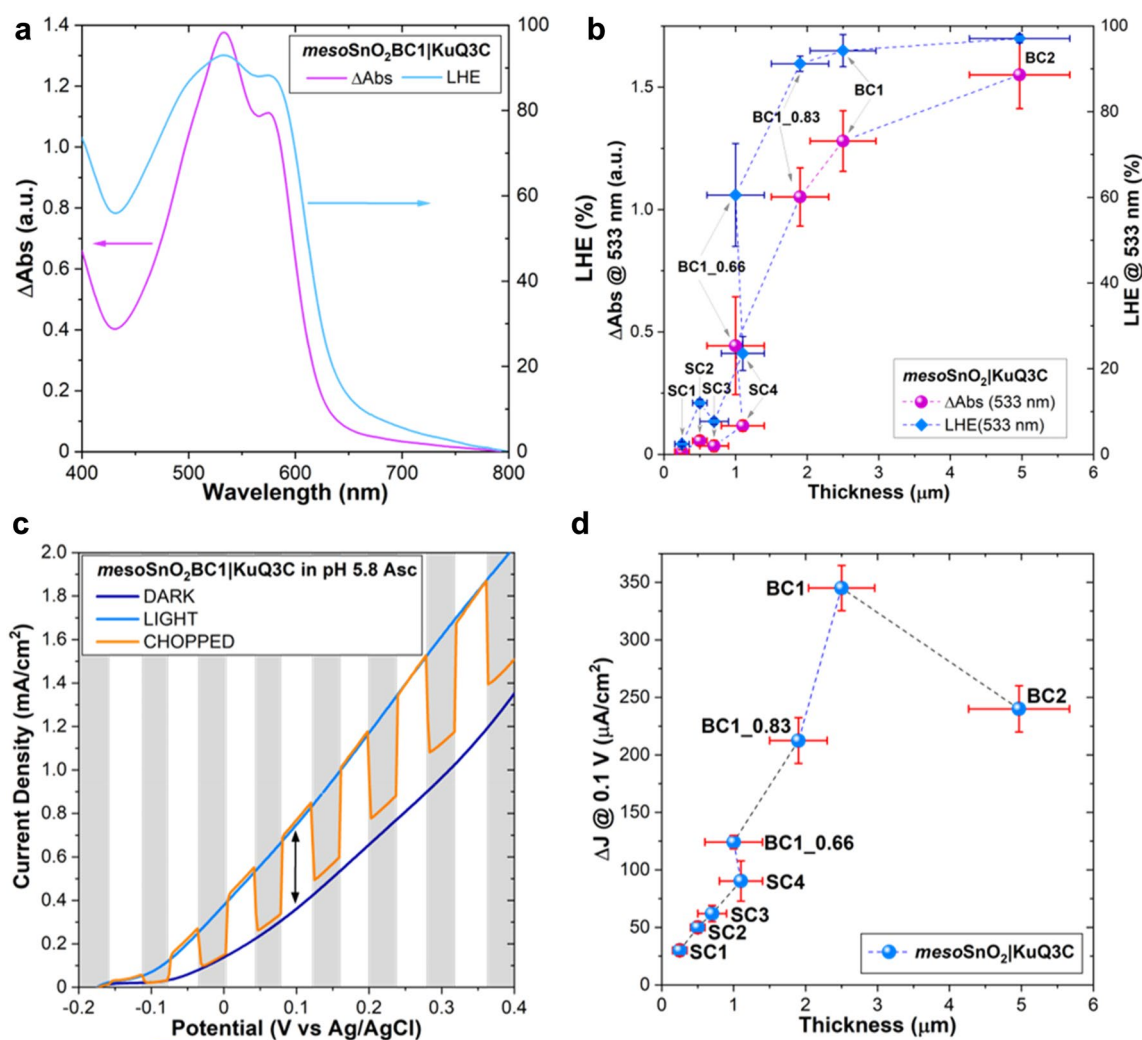
Fig. 2 **a** Absorption spectrum (purple trace) and light-harvesting efficiency (blue trace) of a representative meso-SnO₂|KuQ3C electrode; the spectrum has been subtracted from the blank contribution, due to scattering of SnO₂; a slight red-shift and the inversion of the relative intensity of the two bands of KuQuinone with respect to the spectrum observed in solution are ascribable to dye aggregation on the electrode surface [28]. **b** Plot of the ΔAbs at 533 nm (purple circles) and of LHE (blue diamonds) at 533 nm vs thickness. **c** Chopped linear sweep voltammetries (LSV) of selected photoelectrodes in aqueous ascorbate buffer (pH = 5.8); potentials are reported versus Ag/AgCl; scan rate 20 mV/s. Irradiation was performed with AM 1.5G light (100 mW/cm²) with a cutoff filter at 400 nm [29]. **d** Plot of photocurrent density J at 0.1 V vs electrode thickness; J indicates the net photocurrent density, already subtracted from the dark contribution. The values and error bars associated to ΔAbs, LHE, thickness and J are given as the average value and standard deviation, respectively, among the four samples. The amount of dye per unit surface area can be estimated by the difference in the absorption of the solution (before/after soaking of the electrode) and was previously quantified in 140 ± 20 nmol/cm for meso-SnO₂@KuQ3C electrodes with LHE@533 nm = 90% [29]

rapidly turned purple, owing to protonation of the enolate to the enol form (Fig. S8) [29]. The absorption spectra of the resulting SnO₂|KuQ3C electrodes show the expected features of the KuQuinone dye in the visible region (purple trace in top left of Fig. 2, as a representative spectrum); the absorbance, corrected from the SnO₂ blank, was then converted into the light-harvesting efficiency (LHE) as a key descriptor parameter (LHE(λ) = $1 - 10^{-\text{Abs}(\lambda)}$; azure trace in Fig. 2, top left). The chemisorption of the dye is expected to produce a monolayer, where all the dye molecules are bound to the surface exploiting the anchoring group. Partial aggregation of the dye on the surface is expected from the change of the absorption features on the surface with respect to the solution (broadening of the absorption and change of relative intensity of vibrational peaks).

Focusing on the 533 nm wavelength, which corresponds to the maximum of the absorption, the ΔAbs and the derived value of LHE were observed to depend on the preparation procedure of the SnO₂ substrate, and in particular on the thickness of the SnO₂ layer (Fig. 2 top right).

Indeed, the ΔAbs and the LHE at 533 nm increase almost linearly with the SnO$_2$ thickness up to 2 µm; above this threshold, the ΔAbs@533 tends to a plateau value of ca 1.5 (BC2 electrode in Fig. 2 top right) that corresponds to an LHE@533 around 95% [29]. This saturation-like behaviour is likely ascribable to the inaccessibility of the inner SnO$_2$ layers for binding the organic dye, possibly due to poor permeation of the innermost semiconductor layers by the dye solution. The BC3 electrodes, characterized by the highest thickness, showed mechanical instability during their manipulation for dye chemisorption and were not further considered.

Finally, the use of SnO$_2$ nanorods led to negligible chemisorption of KuQ3C; longer soaking periods, up to 3 days, heating at 50 °C, as well as thermal or chemical pre-treatment of the SnO$_2$ nanorods substrates did not lead to significant improvement of dye uptake (see Supporting Information). This may be either ascribed to the absence of suitable surface sites, or to insufficient surface area of nanorods. Since the contribution of surface Sn–OH groups is clearly visible in the deconvolution of the O 1s XPS region, the undetectable chemisorption of KuQ3C on SnO$_2$ NRs is likely due to the considerably lower density of adsorption sites and smaller surface area typically shown by nanorod morphologies with respect to mesoporous nanostructured films [38]; due to these discouraging results, SnO$_2$ nanorod substrates were not considered for following experiments.

XPS was then performed on meso-SnO$_2$ BC1|KuQ3C as a representative sample (Fig. S9): as expected, the presence of KuQ3C did not influence the Sn 3d (Fig. S9a), Sn 4d (Fig. S9d) core levels and the O–Sn^{4+} component in the O1s region (Fig. S9b); nevertheless, the contribution of the dye is observed in the O1s and C 1s (Fig. S9c) spectra, in terms of (i), the decrease of M–OH and concomitant increase of the C=O/O–C=O peaks in the O1s region, owing to dye chemisorption by condensation between surface hydroxyl groups and carboxylic acid anchors on KuQ3C, and (ii) the marked presence of the C sp^2 component in the C 1s region. The valence band region (Fig. S9d) still shows the fingerprint of SnO$_2$, even though the relative intensity of the three peaks is different with respect to pristine SnO$_2$.

The photoelectrochemical response of meso-SnO$_2$|KuQ3C under anodic scan was tested for the oxidation of ascorbate, in the presence of 0.1 M aqueous ascorbate buffer, pH 5.8 [29]. Linear sweeping voltammetries (LSV) were conducted under dark, light, and chopped conditions (blue, azure, and orange traces in Fig. 2 bottom left are reported for meso-SnO$_2$_BC1|KuQ3C electrodes, as a representative case). Under dark conditions, the rise of a dark anodic current due to oxidation of ascorbate is observed at $E > -0.05$ V vs Ag/AgCl; irradiation leads to an anticipation of the onset potential of ca 0.1 V with respect to dark conditions (onset observed at -0.15 V vs Ag/AgCl),

together with a rise of the photocurrent density J (Fig. 2 bottom left) [46]. In the chopped LSV, the regular rectangular shape of the chopped transients, together with the absence of "bump" anodic photocurrent when irradiation is turned on and the absence of cathodic photocurrent spikes when the irradiation is turned off, is consistent with a fast photoelectrochemical oxidation of ascorbate with negligible surface recombination events [47].

The photocurrent density J observed at 0.1 V vs Ag/AgCl was then employed as the key performance parameter of the photoelectrodes, evaluating its dependence on the semiconductor thickness [48]. The plot of J vs the thickness of SnO$_2$ films shows an increasing trend up to 2 µm (observed for BC1 electrodes), consistent with the increase of LHE of the electrodes. However, an excessive thickness of the SnO$_2$ layer is counterproductive towards the photocurrent response: a ca 50% abatement of photocurrent is indeed observed with KuQ-sensitized BC2 electrodes (5 µm thick), Fig. 2 bottom right [49, 50]; this effect can be explained with the kinetic competition between charge transport and charge recombination, which becomes unfavorable with films exceeding the thickness 2 µm, causing a drop in the electron collection efficiency, mostly due to scattering of the electron with defects, such as grain boundaries between the SnO$_2$ nanoparticles. Therefore, above a certain thickness, the detrimental effect of charge recombination overcomes the beneficial effect of the high light-harvesting efficiency, resulting in the observed photocurrent abatement.

Thus, BC1|KuQ3C electrodes showed the optimal performance in terms of LHE and J; under these conditions, the incident-photon-to-current efficiency (IPCE) showed the expected dependence on the wavelength resembling the LHE trend and peaking at 0.075% at 470 nm (Fig. S10 in Supporting Information). The BC1 meso-SnO$_2$ substrate was thus selected for further investigation.

5 Effect of the anchoring group on the chemisorption onto mesoporous SnO$_2$

The chemisorption of dyes onto semiconductor surfaces, in terms of amount of loading, stability and injection efficiency, is strictly dependent on the nature of the anchoring group employed [51]. Therefore, we evaluated the effect of the length of the alkyl chain (considering 8 vs 3 methylene chain with a carboxylic acid linker) and of the type of anchoring group (considering phosphonic acid vs carboxylic acid, both with 3 methylene chains) of the KuQuinone dyes, see Scheme 1 (the absence of carboxylic or phosphonic acid linkers leads to negligible dye chemisorption onto semiconductor surfaces) [26].

a

b
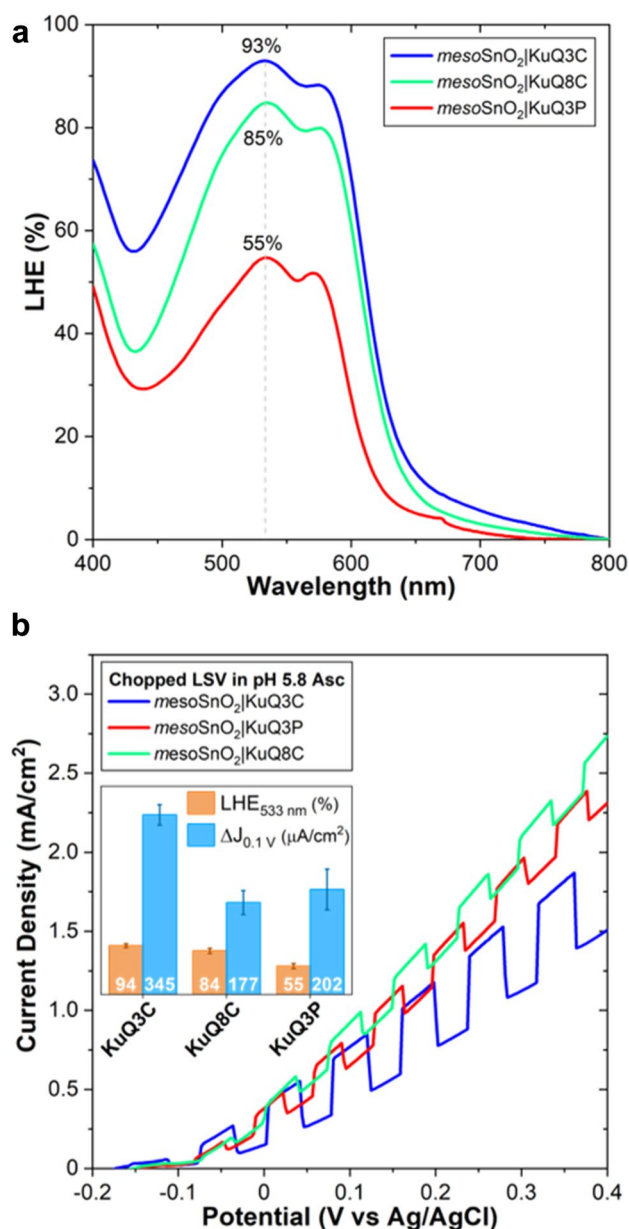
Fig. 3 **a** LHE spectra of meso-SnO$_2$ BC1 electrodes chemisorbed with KuQ3C (blue trace), KuQ8C (green trace) and KuQ3P (red trace). **b** Chopped LSV curves of the same electrodes (scan rate 20 mV/s, same irradiation conditions described in caption of Fig. 2). Inset: histogram plot of LHE at 533 nm (orange bars) and of photocurrent density at 0.1 V vs Ag/AgCl (light blue bars) for the three electrodes (the values and error bars are given as the average value and standard deviation, respectively, among four samples)

BC1 mesoporous SnO$_2$ electrodes, providing the optimal performance with KuQ3C (see previous discussion), were selected for chemisorption of KuQ8C and KuQ3P, following a similar procedure as the one previously described. The resulting electrodes meso-SnO$_2$|KuQ8C and meso-SnO$_2$|KuQ3P were then characterized in terms of LHE and in the photoelectrochemical oxidation of ascorbate (Fig. 3).

Concerning meso-SnO$_2$|KuQ8C, the carboxylic group of the dye allows reaching a similar loading of the dye with respect to the meso-SnO$_2$|KuQ3C (85 vs 93% LHE at 533 nm, Fig. 3a); however, the performance in terms of photocurrent density is 50% abated ($J = 175$ µA/cm^2 for meso-SnO$_2$|KuQ8C vs 350 µA/cm^2 for meso-SnO$_2$|KuQ3C at 0.1 V vs Ag/AgCl, Fig. 3b), suggesting a worse electron transfer between the dye and the semiconductor surface upon increasing the alkyl chain of the anchoring group. In the case of meso-SnO$_2$|KuQ3P, the chemisorption of the dye and the LHE of the electrode are significantly lower with respect to meso-SnO$_2$|KuQ3C (55 vs 93% at 533 nm). The lower loading of the dye is the likely reason of the decreased efficiency in terms of photocurrent density ($J = 200$ µA/cm^2 for meso-SnO$_2$|KuQ3P vs 350 µA/cm^2 for meso-SnO$_2$|KuQ3C).

## 6 Modelling of SnO$_2$|KuQ3C

To elucidate the mechanistic features of electron injection from the dye to the semiconductor, in this section an ab initio modelling of the meso-SnO$_2$|KuQ3C system is proposed and discussed. Electronic structure calculations were performed with density-functional theory (DFT). The reliability of DFT to perform ground state calculations is well known, but the employment of one-electron energy levels (obtained from the solution of Kohn–Sham equations [52] of DFT) as estimates of the quasi-particle energy levels is often problematic. For example, the underestimation of the band gap is a typical feature of DFT results (when hybrid functionals are not employed). Approaches based on many-body perturbation theory (MBPT) lead to better results, but they are computationally more demanding.

With regard to SnO$_2$, many useful data are summarized in the report by Das and Jayaraman [31]. More specifically, stable crystal structures, results of band structure calculations and relative stabilities of low-index surfaces are reported. According to previous findings [53], (110) is the most stable surface and the rutile phase is the most stable crystal structure under standard conditions; therefore in this study, SnO$_2$ was simulated with a slab of two layers where the rutile phase is assumed for the internal structure of the material and the dye is chemisorbed on the (110) surface (the presence of defective sites, and in particular of oxygen vacancies, will also be considered for further studies: defective sites may alter the optical and electronic properties of semiconductor, and the mode of chemisorption of dyes, as documented in the literature [54, 55]).

The computed model involving chemisorption of KuQ3C dye onto the SnO$_2$ slab is indicated as KuQ3C@ SnO$_2$, and its optimized structure is shown in Fig. S11 in the Supporting Information. The KuQ3C chemisorption occurs via a bidentate mode (i.e. a bidentated linker where

Fig. 4 Representation of single occupied molecular orbital (SOMO, α spin) of KuQ3C(H)$^{\bullet}$@SnO$_2$ (left) and of KuQ3C@SnO$_2^-$ (right), the latter representing the state formed after electron injection from the dye to SnO$_2$

SOMO (α spin)
KuQ3C(H)$^{\bullet}$@SnO$_2$

ET to SnO$_2$

-H$^+$
(to solution)

SOMO (α spin)
KuQ3C@SnO$_2^-$
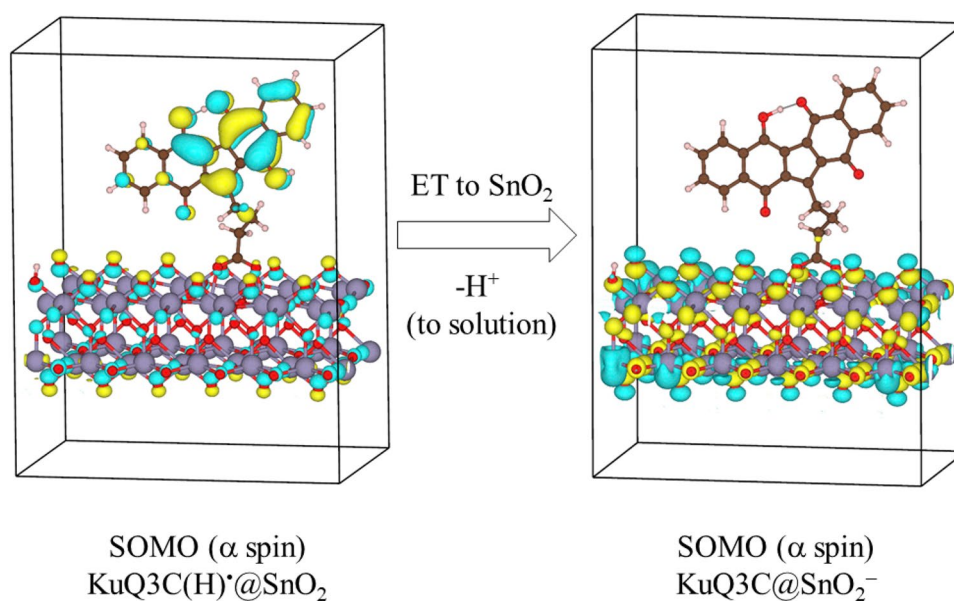
the two carboxylic oxygens of the dye are linked to two tin atoms located at the surface of the SnO$_2$ slab). The proton originally belonging to the carboxylic group of the dye is bound to a surface oxygen of the SnO$_2$ slab [55, 56]. The relevant frontier molecular orbitals and the energy levels of KuQ3C@SnO$_2$ are represented in Fig. S12 in the Supporting Information. The HOMO is localized on the dye, with an analogous shape to the one observed for the HOMO of the isolated dye (Fig. S13 in the SI). The LUMO is located on the SnO$_2$ slab and resembles the LUMO of the isolated slab (i.e. the conduction band of SnO$_2$, Fig. S14 in the SI). Finally, the LUMO+6 of the KuQ3C@SnO$_2$ model corresponds to the LUMO of the isolated dye (Fig. S13 in the SI).
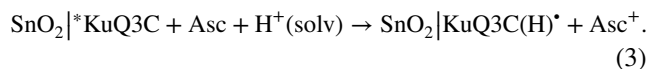
A possible photoinduced electron transfer mechanism involves the electron injection from the excited state of the dye to the conduction band of the SnO$_2$ semiconductor (oxidative quenching, Eqs. 1, 2).

$$SnO_2|KuQ3C + hv \rightarrow SnO_2|^*KuQ3C, \tag{1}$$

$$SnO_2|^*KuQ3C \rightarrow SnO_2^-|KuQ3C^+. \tag{2}$$
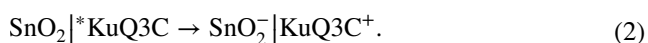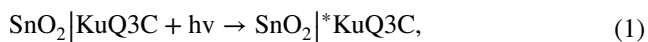
In this scenario, the photoinduced electron transfer is expected to involve the lowest unoccupied orbital localized on the dye (LUMO+6 in KuQ3C@SnO$_2$) and the lowest unoccupied orbital localized on the slab (LUMO in KuQ3C@SnO$_2$). The time for electron injection τ can be roughly estimated by the inverse of the electron coupling strength Γ, for which an approximated measure is the projection of the LUMO+6 broadening on the SnO$_2$ slab (see the equations and further details in Supporting Information) [57, 58]. This analysis provides an estimation of $\tau \sim 0.1$ ps

(100 fs), which is slower than the electron-transfer time calculated for many dyes chemisorbed onto TiO$_2$ [59].

In a previous contribution [29], on the basis of transient absorption spectroscopy evidence, some of us suggested an alternative mechanistic pathway involving the formation of a reduced species of the KuQ3C dye, upon reductive quenching of its excited state with ascorbate, and proceeding via a proton-coupled electron transfer (Eq. 3; the additional proton is indicated as H$^+$(solv) and is provided by the aqueous environment) [29]: this reduced species is thus indicated as KuQ3C(H)$^{\bullet}$, with the additional proton being localized on a second oxygen atom of the polyquinoid scaffold. The calculated absorption spectrum of KuQ3C(H)$^{\bullet}$ and the differential spectrum with respect to the ground state of KuQ3C (Fig. S15 in Supporting Information) nicely match with the experimental transient [29] and further corroborate the assignment.

$$SnO_2|^*KuQ3C + Asc + H^+(solv) \rightarrow SnO_2|KuQ3C(H)^{\bullet} + Asc^+. \tag{3}$$

To investigate a possible role by KuQ3C(H)$^{\bullet}$ in the electron transfer mechanism to SnO$_2$, the structure of the KuQ3C(H)$^{\bullet}$@SnO$_2$ system was optimized and its frontier orbitals were examined. The highest single occupied molecular orbital (SOMO) of KuQ3C(H)$^{\bullet}$@SnO$_2$ is shown in Fig. 4, left panel: the SOMO is mainly delocalized on the organic scaffold of the dye, with a relevant portion located on the oxygen atoms of the SnO$_2$ slab. These features suggest a suitable electronic configuration for electron transfer to SnO$_2$ that restores the dye ground state upon releasing the proton to the aqueous solution (Eq. 4).

$$SnO_2|KuQ3C(H)^{\bullet} \rightarrow SnO_2^-|KuQ3C + H^+(solv). \quad (4)$$

Consistently, the SOMO of KuQ3C@SnO_2^- (i.e. the state after electron injection) is entirely localized on the oxygen atoms of the SnO_2 slab, see Fig. 4 right panel. These results support the important feature of KuQ dyes in managing proton exchange, being relevant in the electron transfer process.

7 Perspectives: photoelectrochemical oxidation of benzyl alcohol

Besides the photoelectrochemical oxidation of ascorbate presented in the previous paragraphs and used as a performance indicator of the electrodes, an emerging approach involves the application of photoanodes for the oxidation of organic compounds aimed at obtaining valuable chemicals [60–64]. In particular, the oxidation of alcohols (dehydrogenation to generate the carbonyl compounds) retains significant interest for the preparation of a multitude of commodity chemicals [65, 66].

The combination of the peculiar PCET redox mechanism and of the powerful oxidizing properties of the excited state enables the possibility of exploiting KuQuinones to perform such type of reactivity; in particular, we selected benzyl alcohol (BA) as a model substrate. A couple of examples of photoanodes for the photoelectrochemical oxidation of BA have been recently reported in the literature, dealing with a $BiVO_4$ based material reported by Berlinguette et al., [65] and a nanostructured TiO_2 or indium tin oxide (ITO) semiconductor decorated with a Ru-polypyridil chromophore and a Ru-based oxidation catalyst reported by Meyer et al. [67].

The meso-SnO_2|KuQ photoanodes were tested towards the photoelectrochemical oxidation of BA both in aqueous and organic medium. In aqueous medium, in the presence of 0.5 M Na_2SO_4 electrolyte [68], an increase in photocurrent density of 10 µA/cm^2 is observed in the 0.5–1.0 V region, upon addition of 1 M BA (Fig. S16 in Supporting Information). This modest photocurrent may be ascribed to the absence of a base able to abstract the two protons that are released in the dehydrogenation of BA. A phosphate aqueous buffer was then considered (0.1 M, pH 6; this is the upper limiting operative pH, since in more basic environment rapid detachment of the dye is observed [29, 51]). Under these conditions, the photocurrent density enhanced by 25 µA/cm^2 upon addition of 0.1 M BA, confirming the beneficial effect of the presence of a proton acceptor (Fig. S16 in Supporting Information).
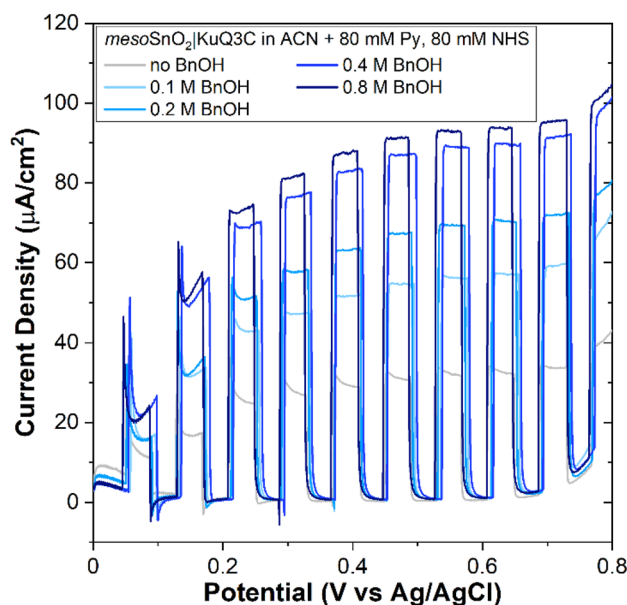
Fig. 5 Photoelectrochemistry of meso-SnO_2|KuQ photoanodes in the presence of BA: chopped LSV in acetonitrile (0.1 M NEt_4BF_4 supporting electrolyte) in the presence of 80 mM pyridine and 80 mM NHS additives, with increasing amount of BA (0–0.8 M): scan rate 20 mV/s. Irradiation was performed with a solar simulator with a cutoff filter at 450 nm, with the electrodes placed at 20 cm distance

However, the most promising results were obtained in organic medium, in particular in acetonitrile solution in the presence of pyridine as a base and *N*-hydroxysuccinimide as a redox mediator, conditions that were previously employed by Berlinguette et al. [65]. Upon addition of increasing concentrations of BA (up to 0.8 M), a progressive enhancement of the photocurrent density is observed in the LSV traces in the potential range between 0 and 0.8 V vs Ag/AgCl (Fig. 5).

In particular, in the potential region below 0.2 V, the chopped *J* transient is characterized by a bump of photocurrent when irradiation is turned on, followed by a rapid relaxation to a steady state photocurrent value; turning off the light leads to the appearance of cathodic current spikes [32]. These features are consistent with the occurrence of recombination events, involving back electron transfer from the SnO_2 semiconductor (electrons in the conduction band or in trapped states) to oxidized species at the electrode surface. The recombination events are contrasted only when a sufficiently positive potential is applied in the scan (*E* > 0.20 V vs Ag/AgCl, Fig. 5 right panel), where the photoanodic transients recover a rectangular shape typical of a fast regenerative cycle, reaching a plateau current density up to 95 µA/cm^2 above 0.5 V at 0.8 M BA concentration (purple trace in Fig. 5). Unfortunately, both the small current density value, together with a progressive dye

detachment during 2 h of electrolysis (held at 0.5 V at the beginning of the plateau region, see Fig. S17 in Supporting Information) prevented the possibility to analyze the oxidation products of BA (most likely benzaldehyde and benzoic acid).

8 Conclusion

We have reported photoelectrodes based on tin oxide semiconductor and pentacyclic KuQuinone dyes. The response of the electrodes towards the photoelectrochemical oxidation of ascorbate depends on the morphology and thickness of the SnO_2 semiconductor and on the anchoring group of the dye. Combining mesoporous SnO_2 layers with 2.5 µm film thickness and a KuQuinone dye with a 3-carboxylpropyl-anchoring chain leads to light-harvesting efficiency of 93% at the maximum absorption wavelength of 533 nm, and photocurrent density J up to 350 µA/cm^2, although with a limited incident photon-to-current efficiency of 0.075%. Performance improvements can be envisaged by enlarging the application of this class of dyes to other semiconductors, and by further engineering the anchoring chain to favour photoinduced electron injection and enhance the stability. As supported by calculations, the proton-coupled electron transfer mechanisms characterizing this class of dyes appears particularly promising for application in photoelectrochemical oxidation of alcohols, as preliminarily investigated in this work for benzyl alcohol substrate. In this perspective, the combination of suitable catalysts could also be considered to enhance the rate of the process.

9 Experimental and computational details

See the Supporting Information for the synthetic procedures of the dyes, preparation and characterization of the electrodes, photoelectrochemical measurements, and computational analysis.

Declarations

Conflict of interest There are no conflicts to declare.

References

1. He, Y., Hamann, T., & Wang, D. (2019). Thin film photoelectrodes for solar water splitting. *Chemical Society Reviews, 48*, 2182–2215.
2. Takata, T., & Domen, K. (2019). Particulate photocatalysts for water splitting: recent advances and future prospects. *ACS Energy Letters, 4*, 542–549.
3. Fujishima, A., Honda, K., Fujishima, A., & Honda, K. (1972). Electrochemical photolysis of water at a semiconductor electrode. *Nature, 238*, 37.
4. Argazzi, R., Murakami Iha, N. Y., Zabri, H., Odobel, F., & Bignozzi, C. A. (2004). Design of molecular dyes for application in photoelectrochemical and electrochromic devices based on nanocrystalline metal oxide semiconductors. *Coordination Chemistry Reviews, 248*, 1299–1316.
5. Kirner, J. T., & Finke, R. G. (2017). Water-oxidation photoanodes using organic light-harvesting materials: a review. *Journal of Materials Chemistry A, 5*, 19560–19592.
6. Crespo-Quesada, M., & Reisner, E. (2017). Emerging approaches to stabilise photocorrodible electrodes and catalysts for solar fuel applications. *Energy & Environmental Science, 10*, 1116–1127.
7. Youngblood, J. W., Lee, S. H. A., Kobayashi, Y., Hernandez-Pagan, E. A., Hoertz, P. G., Moore, T. A., Moore, A. L., Gust, D., & Mallouk, T. E. (2009). Photoassisted overall water splitting in a visible light-absorbing dye-sensitized photoelectrochemical cell. *Journal of the American Chemical Society, 131*, 926–927.
8. Orbelli Biroli, A., Tessore, F., Di Carlo, G., et al. (2019). Fluorinated ZnII porphyrins for dye-sensitized aqueous photoelectrosynthetic cells. *ACS Applied Materials & Interfaces, 11*, 32895–32908.
9. Moore, G. F., Blakemore, J. D., Milot, R. L., Hull, J. F., Song, H., Cai, L., Schmuttenmaer, C. A., Crabtree, R. H., & Brudvig, G. W. (2011). A visible light water-splitting cell with a photoanode formed by codeposition of a high-potential porphyrin and an iridium water-oxidation catalyst. *Energy & Environmental Science, 4*, 2389.
10. Poddutoori, P. K., Thomsen, J. M., Milot, R. L., Sheehan, S. W., Negre, C. F. A., Garapati, V. K. R., Schmuttenmaer, C. A., Batista, V. S., Brudvig, G. W., & Van Der Est, A. (2015). Interfacial electron transfer in photoanodes based on phosphorus(v) porphyrin sensitizers co-deposited on SnO₂ with the Ir(III)Cp∗ water oxidation precatalyst. *Journal of Materials Chemistry A, 3*, 3868–3879.
11. Yamamoto, M., Nishizawa, Y., Chábera, P., Li, F., Pascher, T., Sundström, V., Sun, L., & Imahori, H. (2016). Visible light-driven water oxidation with a subporphyrin sensitizer and a water oxidation catalyst. *Chemical Communications, 52*, 13702–13705.
12. Materna, K. L., Jiang, J., Regan, K. P., Schmuttenmaer, C. A., Crabtree, R. H., & Brudvig, G. W. (2017). Optimization of photoanodes for photocatalytic water oxidation by combining a

heterogenized iridium water-oxidation catalyst with a high-potential porphyrin photosensitizer. *Chemsuschem, 10*, 4526–4534.

13. Suryani, O., Higashino, Y., Mulyana, J. Y., Kaneko, M., Hoshi, T., Shigaki, K., & Kubo, Y. (2017). A near-infrared organic photosensitizer for use in dye-sensitized photoelectrochemical water splitting. *Chemical Communications, 53*, 6784–6787.

14. Bonchio, M., Syrgiannis, Z., Burian, M., et al. (2019). Hierarchical organization of perylene bisimides and polyoxometalates for photo-assisted water oxidation. *Nature Chemistry, 11*, 146–153.

15. Ronconi, F., Syrgiannis, Z., Bonasera, A., Prato, M., Argazzi, R., Caramori, S., Cristino, V., & Bignozzi, C. A. (2015). Modification of nanocrystalline WO_3 with a dicationic perylene bisimide: applications to molecular level solar water splitting. *Journal of the American Chemical Society, 137*, 4630–4633.

16. Kirner, J. T., Stracke, J. J., Gregg, B. A., & Finke, R. G. (2014). Visible-light-assisted photoelectrochemical water oxidation by thin films of a phosphonate-functionalized perylene diimide plus CoO_x cocatalyst. *ACS Applied Materials & Interfaces, 6*, 13367–13377.

17. Kirner, J. T., & Finke, R. G. (2017). Sensitization of nanocrystalline metal oxides with a phosphonate-functionalized perylene diimide for photoelectrochemical water oxidation with a CoO_x catalyst. *ACS Applied Materials & Interfaces, 9*, 27625–27637.

18. Berardi, S., Cristino, V., Canton, M., et al. (2017). Perylene diimide aggregates on Sb-doped SnO_2: charge transfer dynamics relevant to solar fuel generation. *Journal of Physical Chemistry C, 121*, 17737–17745.

19. Wee, K. R., Sherman, B. D., Brennaman, M. K., Sheridan, M. V., Nayak, A., Alibabaei, L., & Meyer, T. J. (2016). An aqueous, organic dye derivatized SnO_2/TiO_2 core/shell photoanode. *Journal of Materials Chemistry A, 4*, 2969–2975.

20. Li, F., Fan, K., Xu, B., Daniel, Q., Sun, L., Li, L., & Gabrielsson, E. (2015). Organic dye-sensitized tandem photoelectrochemical cell for light driven total water splitting. *Journal of the American Chemical Society, 137*, 9153–9159.

21. Bornoz, P., Prévot, M. S., Yu, X., Guijarro, N., & Sivula, K. (2015). Direct light-driven water oxidation by a ladder-type conjugated polymer photoanode. *Journal of the American Chemical Society, 137*, 15338–15341.

22. Chen, J., Wagner, P., Tong, L., Wallace, G. G., Officer, D. L., & Swiegers, G. F. (2012). A porphyrin-doped polymer catalyzes selective, light-assisted water oxidation in seawater. *Angewandte Chemie International Edition, 51*, 1907–1910.

23. Chen, J., Wagner, P., Tong, L., Boskovic, D., Zhang, W., Officer, D., Wallace, G. G., & Swiegers, G. F. (2013). A light-assisted, polymeric water oxidation catalyst that selectively oxidizes seawater with a low onset potential. *Chemical Science, 4*, 2797.

24. Valentini, F., Sabuzi, F., Conte, V., Nemykin, V. N., & Galloni, P. (2021). Unveiling KuQuinone redox species: an electrochemical and computational cross study. *Journal of Organic Chemistry, 86*, 5680–5689.

25. Coletti, A., Lentini, S., Conte, V., Floris, B., Bortolini, O., Sforza, F., Grepioni, F., & Galloni, P. (2012). Unexpected one-pot synthesis of highly conjugated pentacyclic diquinoid compounds. *Journal of Organic Chemistry, 77*, 6873–6879.

26. Bonomo, M., Sabuzi, F., Di Carlo, A., Conte, V., Dini, D., & Galloni, P. (2017). KuQuinones as sensitizers for NiO based p-type dye-sensitized solar cells. *New Journal of Chemistry, 41*, 2769–2779.

27. Sabuzi, F., Lentini, S., Sforza, F., Pezzola, S., Fratelli, S., Bortolini, O., Floris, B., Conte, V., & Galloni, P. (2017). KuQuinones equilibria assessment for biomedical applications. *Journal of Organic Chemistry, 82*, 10129–10138.

28. Sabuzi, F., Armuzza, V., Conte, V., Floris, B., Venanzi, M., Galloni, P., & Gatto, E. (2016). KuQuinones: a new class of quinoid compounds as photoactive species on ITO. *Journal of Materials Chemistry C, 4*, 622–629.

29. Volpato, G. A., Marasi, M., Gobbato, T., et al. (2020). Photoanodes for water oxidation with visible light based on a pentacyclic quinoid organic dye enabling proton-coupled electron transfer. *Chemical Communications, 56*, 2248–2251.

30. Forchetta, M., Conte, V., Fiorani, G., Galloni, P., & Sabuzi, F. (2021). A sustainable improvement of ω-bromoalkylphosphonates synthesis to access novel KuQuinones. *Organics, 2*, 107–117.

31. Das, S., & Jayaraman, V. (2014). SnO_2: A comprehensive review on structures and gas sensors. *Progress in Materials Science, 66*, 112–255.

32. Benazzi, E., Rettenmaier, K., Berger, T., Caramori, S., Berardi, S., Argazzi, R., Prato, M., & Syrgiannis, Z. (2020). Photoelectrochemical properties of SnO_2 photoanodes sensitized by cationic perylene-di-imide aggregates for aqueous HBr splitting. *Journal of Physical Chemistry C, 124*, 1317–1329.

33. Hernández-Alonso, M. D., Fresno, F., Suárez, S., & Coronado, J. M. (2009). Development of alternative photocatalysts to TiO_2: challenges and opportunities. *Energy & Environmental Science, 2*, 1231–1257.

34. Li, X., Yu, J., Low, J., Fang, Y., Xiao, J., & Chen, X. (2015). Engineering heterogeneous semiconductors for solar water splitting. *Journal of Materials Chemistry A, 3*, 2485–2534.

35. Li, Z., Luo, W., Zhang, M., Feng, J., & Zou, Z. (2013). Photoelectrochemical cells for solar hydrogen production: current state of promising photoelectrodes, methods to improve their properties, and outlook. *Energy & Environmental Science, 6*, 347–370.

36. Zainudin, S. N. F., Abdullah, H., & Markom, M. (2019). Electrochemical studies of tin oxide based-dye-sensitized solar cells (DSSC): a review. *Journal of Materials Science: Materials in Electronics, 30*, 5342–5356.

37. Salmaoui, S., Sediri, F., Gharbi, N., Perruchot, C., Aeiyach, S., Rutkowska, I. A., Kulesza, P. J., & Jouini, M. (2011). Hexagonal nanorods of tungsten trioxide: synthesis, structure, electrochemical properties and activity as supporting material in electrocatalysis. *Applied Surface Science, 257*, 8223–8229.

38. Dong, H., Wang, L., Gao, R., Ma, B., & Qiu, Y. (2011). Constructing nanorod–nanoparticles hierarchical structure at low temperature as photoanodes for dye-sensitized solar cells: combining relatively fast electron transport and high dye-loading together. *Journal of Materials Chemistry, 21*, 19389–19394.

39. Liu, B., & Aydil, E. S. (2009). Growth of oriented single-crystalline rutile TiO_2 nanorods on transparent conducting substrates for dye-sensitized solar cells. *Journal of the American Chemical Society, 131*, 3985–3990.

40. Chen, Z., Pan, D., Li, Z., Jiao, Z., Wu, M., Shek, C. H., Wu, C. M. L., & Lai, J. K. L. (2014). Recent advances in tin dioxide materials: some developments in thin films, nanowires, and nanorods. *Chemical Reviews, 114*, 7442–7486.

41. Vayssieres, L., & Graetzel, M. (2004). Highly ordered SnO_2 nanorod arrays from controlled aqueous growth. *Angewandte Chemie International Edition, 43*, 3666–3670.

42. Szuber, J., Czempik, G., Larciprete, R., Koziej, D., & Adamowicz, B. (2001). XPS study of the L-CVD deposited SnO_2 thin films exposed to oxygen and hydrogen. *Thin Solid Films, 391*, 198–203.

43. Themlin, J.-M., Chtaib, M., Henrard, L., Lambin, P., Darville, J., & Gilles, J.-M. (1992). Characterization of tin oxides by X-ray-photoemission spectroscopy. *Physical Review B, 46*, 2460–2466.

44. Kövér, L., Kovács, Z., Sanjinés, R., Moretti, G., Cserny, I., Margaritondo, G., Pálinkás, J., & Adachi, H. (1995). Electronic structure of tin oxides: high-resolution study of XPS and Auger spectra. *Surface and Interface Analysis, 23*, 461–466.

45. Moulder, J. F., Stickle, W. F., Sobol, P. E., & Bomben, K. D. (1992). *Handbook of X-ray photoelectron spectroscopy*. Waltham: Perkin-Elmer.

46. Lai, Y.-H., Kato, M., Mersch, D., & Reisner, E. (2014). Comparison of photoelectrochemical water oxidation activity of a synthetic photocatalyst system with photosystem II. *Faraday Discussions, 00*, 1–13.

47. Li, J., Wan, W., Triana, C. A., Novotny, Z., Osterwalder, J., Erni, R., & Patzke, G. R. (2019). Dynamic role of cluster cocatalysts on molecular photoanodes for water oxidation. *Journal of the American Chemical Society, 141*, 12839–12848.

48. Mersch, D., Lee, C. Y., Zhang, J. Z., Brinkert, K., Fontecilla-Camps, J. C., Rutherford, A. W., & Reisner, E. (2015). Wiring of photosystem II to hydrogenase for photoelectrochemical water splitting. *Journal of the American Chemical Society, 137*, 8541–8549.

49. Hernández, S., Saracco, G., Barbero, G., & Alexe-Ionescu, A. L. (2017). Role of the electrode morphology on the optimal thickness of $BiVO_4$ anodes for photoelectrochemical water splitting cells. *Journal of Electroanalytical Chemistry, 799*, 481–486.

50. Murakami, N., & Watanabe, R. (2020). Simultaneous measurements of photoabsorption and photoelectrochemical performance for thickness optimization of a semiconductor photoelectrode. *ACS Combinatorial Science, 22*, 791–795.

51. Materna, K. L., Crabtree, R. H., & Brudvig, G. W. (2017). Anchoring groups for photocatalytic water oxidation on metal oxide surfaces. *Chemical Society Reviews, 46*, 6099–6110.

52. Kohn, W., & Sham, L. J. (1965). Self-consistent equations including exchange and correlation effects. *Physical Review, 140*, A1133–A1138.

53. Oviedo, J., & Gillan, M. J. (2000). Energetics and structure of stoichiometric SnO_2 surfaces studied by first-principles calculations. *Surface Science, 463*, 93–101.

54. Gerosa, M., Bottani, C. E., Caramella, L., Onida, G., Di Valentin, C., & Pacchioni, G. (2015). Defect calculations in semiconductors through a dielectric-dependent hybrid DFT functional: the case of oxygen vacancies in metal oxides. *The Journal of Chemical Physics*. https://doi.org/10.1063/1.4931805

55. Orellana, W. (2021). D-π-A dye attached on $TiO_2(101)$ and $TiO_2(001)$ surfaces: electron transfer properties from ab initio calculations. *Solar Energy, 216*, 266–273.

56. Khishigjargal, T., Javkhlantugs, N., Ganzorig, C., Kurihara, Y., Sakomura, M., & Ueda, K. (2013). Density functional study of the cluster model of $SnO_2(110)$ surface modified by benzoic acids. *World Journal of Nano Science and Engineering, 03*, 52–56.

57. Persson, P., Lundqvist, M. J., Ernstorfer, R., Goddard, W. A., & Willig, F. (2006). Quantum chemical calculations of the influence of anchor-cum-spacer groups on femtosecond electron transfer times in dye-sensitized semiconductor nanocrystals. *Journal of Chemical Theory and Computation, 2*, 441–451.

58. Martsinovich, N., & Troisi, A. (2011). High-throughput computational screening of chromophores for dye-sensitized solar cells. *Journal of Physical Chemistry C, 115*, 11781–11792.

59. Umari, P., Giacomazzi, L., De Angelis, F., Pastore, M., & Baroni, S. (2013). Energy-level alignment in organic dye-sensitized TiO2 from GW calculations. *The Journal of Chemical Physics, 139*, 014709.

60. You, B., Liu, X., Jiang, N., & Sun, Y. (2016). A general strategy for decoupled hydrogen production from water splitting by integrating oxidative biomass valorization. *Journal of the American Chemical Society, 138*, 13639–13646.

61. Reid, L. M., Li, T., Cao, Y., & Berlinguette, C. P. (2018). Organic chemistry at anodes and photoanodes. *Sustain Energy Fuels, 2*, 1905–1927.

62. Ru Ng, A. Y., Boruah, B., Chin, K. F., Modak, J. M., & Sen, S. H. (2020). Photoelectrochemical cells for artificial photosynthesis: alternatives to water oxidation. *ChemNanoMat, 6*, 185–203.

63. Wild, U., Schön, F., & Himmel, H. J. (2017). Oxidation of organic molecules with a redox-active guanidine catalyst. *Angewandte Chemie International Edition, 56*, 16410–16413.

64. Kuttassery, F., Mathew, S., Remello, S. N., Thomas, A., Sano, K., Ohsaki, Y., Nabetani, Y., Tachibana, H., & Inoue, H. (2018). Alternative route to bypass the bottle-neck of water oxidation: two-electron oxidation of water catalyzed by earth-abundant metalloporphyrins. *Coordination Chemistry Reviews, 377*, 64–72.

65. Li, T., Kasahara, T., He, J., Dettelbach, K. E., Sammis, G. M., & Berlinguette, C. P. (2017). Photoelectrochemical oxidation of organic substrates in organic media. *Nature Communications, 8*, 6–10.

66. Das, A., & Stahl, S. S. (2017). Noncovalent immobilization of molecular electrocatalysts for chemical synthesis: efficient electrochemical alcohol oxidation with a pyrene–TEMPO conjugate. *Angewandte Chemie International Edition, 56*, 8892–8897.

67. Song, W., Vannucci, A. K., Farnum, B. H., et al. (2014). Visible light driven benzyl alcohol dehydrogenation in a dye-sensitized photoelectrosynthesis cell. *Journal of the American Chemical Society, 136*, 9773–9779.

68. Zhang, R., Shao, M., Li, Z., Ning, F., Wei, M., Evans, D. G., & Duan, X. (2017). Photoelectrochemical catalysis toward selective anaerobic oxidation of alcohols. *Chemistry—A European Journal, 23*, 8142–8147.